ISSN: 2710-0588

Thermal Analysis of a Hollow-Shaft Water-Cooled Permanent-Magnet Motor

Wenzheng Liu

School of Shandong Jiaotong University, Jinan 250000, China

Abstract

With the increasing demand for compact, high-power-density underwater propulsion systems, heat dissipation in permanent-magnet motors has become an increasingly important issue, and cooling performance directly affects motor service life and operational safety. Conventional approaches, including housing water jackets, air cooling, and hybrid cooling, may involve long heat-transfer paths, structural redundancy, or limited cooling capacity. This study proposes an internal cooling structure based on a hollow shaft, integrating the coolant passage with the rotor shaft system to shorten the rotor-side heat-transfer path while improving heat dissipation and maintaining compactness and engineering applicability. Computational fluid dynamics (CFD) is used to calculate the temperature fields of a permanent-magnet motor with different water-channel configurations under rated operating conditions. The results show that the smooth axial channel provides better overall hydraulic and thermal performance than the helical channel: its maximum temperature is 26.24 °C, compared with 27.04 °C for the helical channel, while the maximum inlet–outlet pressure difference decreases from 1058 Pa to 163 Pa. With a 50-mm hollow-shaft cooling channel, the maximum temperatures of the stator core, winding, permanent magnet, and shaft are 63.34 °C, 68.03 °C, 30.86 °C, and 34.25 °C, respectively, substantially below those of the solid-shaft baseline, in which all key components exceed 247 °C. These results indicate that a hollow-shaft cooling design with a smooth axial channel can improve heat removal from the rotor region and reduce the risk of permanent-magnet overheating under the investigated conditions.

Keywords

Permanent-magnet propulsion motor; hollow shaft; water cooling; cooling-channel geometry; computational fluid dynamics; thermal analysis.

1. Introduction

Permanent-magnet motors are widely used in electric propulsion systems, specialized equipment, and underwater propulsion because of their high power density, compact size, and favorable dynamic response. However, as applications expand and electromagnetic loading and current density increase, winding copper losses, core losses, and local eddy-current losses also rise. Heat dissipation has therefore become a key factor limiting motor efficiency and service life [1–3]. Accordingly, selecting an appropriate cooling method and achieving stable, efficient heat removal within existing structural constraints are important directions in the design and optimization of permanent-magnet motors.

Several cooling approaches—including water, air, oil, and hybrid cooling—have been investigated. Water cooling is considered one of the most promising options for high-power-density permanent-magnet motors because of its high heat-transfer capacity and structural adaptability [1,4]. Tang et al. [5] investigated heat-transfer paths and temperature-rise distributions in a water-cooled permanent-magnet synchronous machine using an equivalent

ISSN: 2710-0588

thermal-conductance model. Jeon et al. [6] analyzed how water-jacket channel layout, flow rate, and inlet/outlet positions affect cooling performance. Zhao et al. [7] optimized the thermal performance and pressure-drop characteristics of a spiral cooling channel, showing that an appropriate channel geometry can enhance heat transfer while controlling pressure losses. Chen et al. [8] proposed a dual-channel internal-circulation water-cooling structure for a permanent-magnet synchronous motor used in an underwater unmanned vehicle. At a flow rate of 6 L/min, the maximum operating temperature was reduced by 51.72 K and the maximum temperature-rise suppression rate reached 53.02%, demonstrating the advantages of internal liquid cooling in a sealed system. Wang et al. [9] reported that permanent magnets are temperature-sensitive components in water-cooled, low-speed outer-rotor motors because of their long heat-transfer paths. Their optimized circumferential Z-shaped water-cooling structure reduced the maximum temperatures of the permanent magnets, stator core, and stator windings to 89.14 °C, 50.36 °C, and 50.17 °C, respectively, while also reducing the pressure drop. These studies highlight the importance of cooling-channel topology, flow-rate matching, and hotspot suppression in the rotor region [8,9].

Although considerable progress has been made in housing water jackets, spiral channels, Z-shaped passages, and internal liquid-cooling systems, research specifically addressing hollow-shaft water-cooled permanent-magnet propulsion motors remains limited. Previous studies have examined hollow-shaft rotor cooling in interior permanent-magnet motors [10], broader thermal-management strategies for electric machines [11], direct liquid cooling [12], and thermal-modeling techniques for permanent-magnet machines [13]. More recent work has investigated validated direct-rotor cooling and the trade-offs of direct liquid cooling in compact machines [14,15]. Nevertheless, the effects of channel topology, radial channel diameter, and coolant velocity on the overall temperature field of the propulsion motor considered here require further systematic evaluation. Underwater propulsion motors must also satisfy constraints on compactness, housing sealing, continuous loading, and system integration, so a conventional housing-only water jacket may not fully meet practical requirements [8,9].

This study investigates a hollow-shaft water-cooled permanent-magnet propulsion motor by combining electromagnetic-loss calculations, flow analysis, and numerical temperature-field simulation. The temperature distributions are examined under different channel geometries, radial channel diameters, and coolant velocities, with particular attention to the temperature rise of the permanent magnets, windings, and core. The hollow shaft provides additional space for coolant flow and internal channel layout, potentially shortening the heat-transfer paths from the rotor and permanent magnets and mitigating the conventional problem that the stator is easier to cool than the rotor. The findings may provide a theoretical basis for optimizing the cooling structure and improving the safe, stable operation of high-power-density permanent-magnet propulsion motors.

2. Motor Parameters and Physical Model

2.1. Physical Model and Basic Parameters

The investigated machine is a 1.5-kW interior-rotor permanent-magnet motor. It mainly consists of a stator core, stator windings, permanent magnets, a hollow shaft, a housing, and internal cooling channels. Compared with a conventional solid shaft, the hollow shaft provides internal space for coolant flow while maintaining torque transmission, which can enhance rotor-side heat removal and improve the internal temperature distribution. The basic design parameters are listed in Table 1, and the three-dimensional physical model constructed from these parameters is shown in Fig. 1.

ISSN: 2710-0588

Table 1. Basic parameters of the permanent-magnet motor

Parameter	Value	Remarks
Rated power (W)	1500	
Rated speed (r/min)	3900	
Number of stator slots	12	
Number of pole pairs	4	
Permanent-magnet grade	NdFe35	Allowable temperature: 80 °C
Insulation class	B	Allowable temperature: 130 °C
Air-gap length (mm)	0.5	
Core length (mm)	95	
Magnetization-direction length (mm)	4	

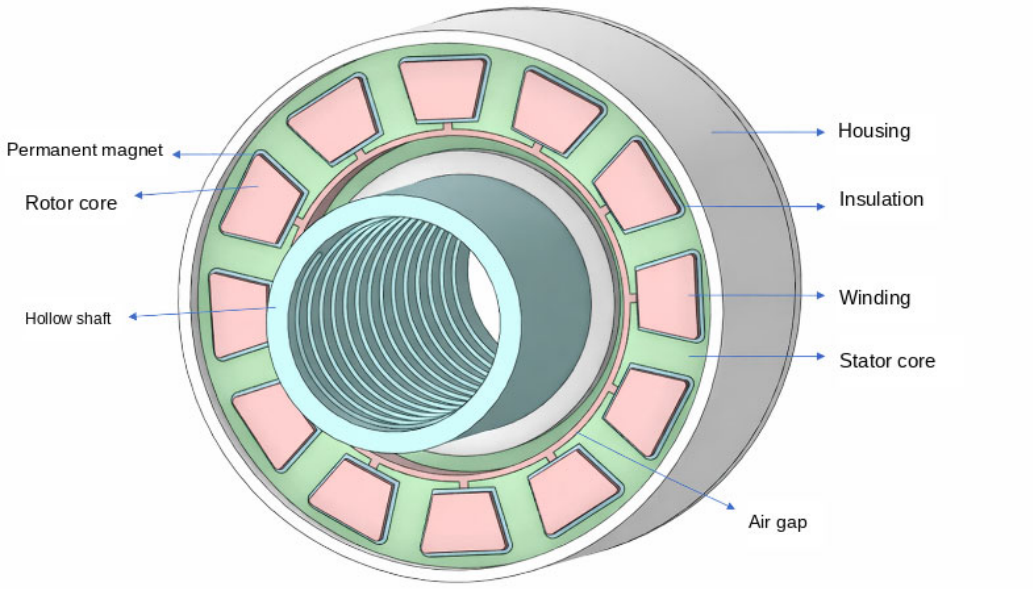


Figure 1. Physical model of the motor

2.2. Cooling Structure and Heat-Transfer Path

During motor operation, stator-winding copper losses, stator-core iron losses, and permanent-magnet eddy-current losses are continuously converted into heat and constitute the main sources of temperature rise. The stator windings and stator core are close to the housing and cooling boundary, so heat can be conducted outward through the core, slot insulation, and housing. By contrast, the rotor and permanent-magnet regions have longer heat-transfer paths to the external cooling boundary and are therefore more prone to local hotspots. For permanent-magnet propulsion motors, excessive magnet temperature increases the risk of demagnetization; rotor-side thermal management is consequently a major focus of temperature-field analysis.

The internal cooling structure of the hollow shaft changes the conventional heat-dissipation path, allowing heat from the rotor and permanent-magnet regions to be transferred more directly to the coolant. This shortens the heat-transfer path and reduces thermal resistance. Accordingly, an electromagnetic-loss, fluid-flow, and temperature-field coupled model is established based on the physical motor model to investigate the effect of hollow-shaft water cooling on the motor temperature distribution.

ISSN: 2710-0588

3. Mathematical Model and Boundary Conditions

3.1. Basic Assumptions and Heat-Source Model

To improve computational efficiency and maintain engineering applicability, the following assumptions are made in the temperature-field model:

1) The motor operates under steady-state rated conditions, and the thermophysical properties of each component are treated as constants.

2) The stator windings are represented by an equivalent solid model; skin and proximity effects are neglected.

3) The stator core is represented by an equivalent thermal-conduction model, and the laminated core is treated as an anisotropic conducting medium.

4) The main heat sources are stator-winding copper losses, stator-core iron losses, and permanent-magnet eddy-current losses; mechanical and additional losses are neglected.

5) The coolant flows through the hollow-shaft channel as an incompressible, steady flow, and thermal radiation is neglected.

6) The housing is simplified as a cylindrical structure, and the thermal influence of the bearings is neglected.

7) Within the seawater domain, the motor housing is treated as a constant-temperature wall at 20 °C.

The total motor loss can be expressed as

$$P_{loss} = P_{Cu} + P_{Fe,s} + P_{pm} \tag{1}$$

Where P_{Cu} denotes the stator-winding copper loss, $P_{Fe,s}$ denotes the stator-core iron loss, P_{pm} denotes the permanent-magnet eddy-current loss. The stator-winding copper loss is given by

$$P_{Cu} = mI^2R \tag{2}$$

Where m denotes the number of phases, I is the RMS phase current, R is the phase resistance.

To apply heat sources in the temperature-field model, the losses of each component are represented as uniform volumetric heat sources, i.e.,

$$q_v = \frac{P}{V} \tag{3}$$

Where q_v is the volumetric heat-generation rate, P is the loss of the corresponding component, V is the effective volume of the corresponding component. Based on the electromagnetic-field simulation results, the losses of the windings, stator core, rotor core, and permanent magnets are assigned to their respective regions. Because the hollow-shaft structure changes the rotor-side heat-transfer path, the temperature rise of the rotor and permanent-magnet regions is the focus of the subsequent analysis.

A two-dimensional motor model is established in Ansys Maxwell, and electromagnetic-field simulation is used to obtain the stator-core iron loss, stator-winding copper loss, and permanent-magnet eddy-current loss. The losses and volumetric heat-generation rates of the motor components are listed in Table 2.

ISSN: 2710-0588

Table 2. Loss distribution

Component	Loss (W)	Volumetric heat-generation rate ($W \cdot m^{-3}$)
Stator windings	145.2	512647.3
Stator core	136.8	365122.7
Permanent magnets	81	1715770.5

3.2. Governing Equations

3.2.1. Heat Conduction in the Solid Domain

Under steady-state conditions, heat conduction in the solid domain of the motor is governed by the three-dimensional heat-conduction equation:

$$\frac{\partial}{\partial x}\left(k_x \frac{\partial T}{\partial x}\right) + \frac{\partial}{\partial y}\left(k_y \frac{\partial T}{\partial y}\right) + \frac{\partial}{\partial z}\left(k_z \frac{\partial T}{\partial z}\right) + q_v = 0 \tag{4}$$

Where T is the temperature, k_x, k_y and k_z are the thermal conductivities of the material in the three coordinate directions, $q_v$is the volumetric heat-generation rate.

For isotropic materials,

$$k_x = k_y = k_z = k \tag{5}$$

The heat-conduction equation can be simplified to

$$k\left(\frac{\partial^2 T}{\partial x^2} + \frac{\partial^2 T}{\partial y^2} + \frac{\partial^2 T}{\partial z^2}\right) + q_v = 0 \tag{6}$$

3.2.2. Governing Equations for the Fluid Domain

The coolant flow and heat transfer in the internal hollow-shaft channel satisfy the conservation equations for mass, momentum, and energy.

The continuity equation is

$$\nabla \cdot u = 0 \tag{7}$$

In component form, it can be written as

$$\frac{\partial u}{\partial x} + \frac{\partial v}{\partial y} + \frac{\partial w}{\partial z} = 0 \tag{8}$$

The momentum equation is

$$\rho\,(u \cdot \nabla)u = -\nabla\, p + \mu\, \nabla^2 u + F \tag{9}$$

Where $\rho$is the fluid density, $u$is the velocity vector, $p$is the pressure, $\mu$is the dynamic viscosity, $F$and the body-force term.

The energy equation is

$$\rho\, c_p\, (u \cdot \nabla\, T) = \nabla \cdot (\lambda\, \nabla\, T) + S_T \tag{10}$$

ISSN: 2710-0588

Where c_p is the specific heat capacity, λ is the thermal conductivity of the fluid, and S_T is the energy-source term. For the coolant-flow problem considered here, the source term is usually set to $S_T = 0$.

3.2.3. Turbulence Model

To enhance heat transfer, the coolant flowing through the hollow-shaft channel is generally turbulent, and its Reynolds number is

$$Re = \frac{\rho v D_h}{\mu} \tag{11}$$

Where v is the characteristic flow velocity, and D_h is the hydraulic diameter of the channel.

Considering the pronounced near-wall heat transfer in the hollow-shaft channel and the possibility of local flow separation, the $SST\ k-\omega$ turbulence model is used to solve the coolant-flow and heat-transfer processes. The transport equation for turbulent kinetic energy k is given by

$$\frac{\partial(\rho k)}{\partial t} + \frac{\partial(\rho k u_i)}{\partial x_i} = \frac{\partial}{\partial x_j}\left[(\mu + \sigma_k \mu_t)\frac{\partial k}{\partial x_j}\right] + G_k - Y_k \tag{12}$$

The transport equation for the specific dissipation rate ω is

$$\frac{\partial(\rho \omega)}{\partial t} + \frac{\partial(\rho \omega u_i)}{\partial x_i} = \frac{\partial}{\partial x_j}\left[(\mu + \sigma_\omega \mu_t)\frac{\partial \omega}{\partial x_j}\right] + G_\omega - Y_\omega + D_\omega \tag{13}$$

Where k denotes the turbulent kinetic energy, ω denotes the specific dissipation rate, ρ denotes the fluid density, u_i denotes the velocity components, x_i and x_j denote the spatial coordinates, t denotes time, μ denotes the dynamic viscosity of the fluid, μ_t denotes the turbulent viscosity, σ_k and σ_ω are model constants in the turbulent-kinetic-energy and specific-dissipation-rate equations, respectively. G_k denotes the production term of turbulent kinetic energy caused by the mean velocity gradient, G_ω denotes the production term of specific dissipation rate, Y_k and Y_ω denote the dissipation terms for turbulent kinetic energy and specific dissipation rate, respectively, D_ω denotes the cross-diffusion term, which describes the coupling between the $k-\omega$ model and the $k-\varepsilon$ model in the transition region.

$SST\ k-\omega$ model uses the $k-\omega$ model formulation, which describes near-wall flow and heat transfer well; farther from the wall, the flow gradually transitions to the $k-\varepsilon$ model formulation, thereby balancing near-wall accuracy and stability in the core flow. Therefore, this model is suitable for complex flow and heat-transfer problems in hollow-shaft channels, where near-wall heat transfer is significant and local flow separation may occur.

3.3. Boundary Conditions and Equivalent Treatments

The losses in the motor's heat-source regions are obtained from electromagnetic-field calculations and applied as volumetric heat sources to the windings, stator core, and permanent magnets. At the contact interface between the coolant and the inner wall of the hollow shaft, fluid–solid coupling boundary conditions are applied. First, the temperature is continuous across the fluid–solid interface, i.e.,

$$T_f = T_s \tag{14}$$

Second, the normal heat flux is continuous across the interface, i.e.,

ISSN: 2710-0588

$$-\lambda_f \frac{\partial T_f}{\partial n} = -\lambda_s \frac{\partial T_s}{\partial n} \tag{15}$$

Where T_f and T_s denote the fluid-side and solid-side interface temperatures, λ_f and λ_s denote the thermal conductivities of the fluid and solid, respectively, and n is the interface normal direction. For convective heat transfer between the external surface and the surroundings,

$$-\frac{k(\partial T)}{\partial n} = h(T - T_\infty) \tag{16}$$

Where h is the convective heat-transfer coefficient, T_∞ is the ambient temperature. If the motor housing is directly exposed to external seawater, the convective heat-transfer coefficient between the housing and seawater is set according to the operating conditions. If the focus is on internal cooling, the external surface may instead be modeled using a natural-convection or adiabatic boundary.

To reduce model complexity, the stator windings are treated using an equivalent thermal-conduction model, whose axial equivalent thermal conductivity is

$$\lambda_{eq,a} = \lambda_{Cu}\eta + \lambda_{ins}(1 - \eta) \tag{17}$$

Where λ_{Cu} is the thermal conductivity of copper, λ_{ins} is the thermal conductivity of the insulation, and η is the slot fill factor. The laminated stator core is treated as an anisotropic conducting medium, and the equivalent thermal-conductivity method is used to represent heat transfer across the air gap.

In summary, a coupled model of electromagnetic losses, fluid flow, and temperature field is established for the hollow-shaft water-cooled permanent-magnet propulsion motor. Appropriate boundary conditions are applied to numerically analyze the internal temperature distribution and cooling performance.

3.4. Thermophysical Properties of the Main Materials

The thermal performance of a water-cooled motor depends on the thermophysical properties of its conducting media, the flow regime, and the convective heat-transfer conditions. Material properties are determined by the materials themselves, whereas the flow regime and heat-transfer coefficient are closely related to channel geometry and cooling conditions. The principal thermophysical properties used in the temperature-field calculations are listed in Table 3.

Table 3. Thermophysical properties of the main motor materials

Component	Material	Density ($kg \cdot m^{-3}$)	Specific heat capacity ($J \cdot kg^{-1} \cdot K^{-1}$)	Thermal conductivity ($W \cdot m^{-1} \cdot K^{-1}$)
Stator core	DW3150	7650	460	25
Stator windings	Copper	6500	385	390
Hollow shaft	Grade 50 steel	7850	460	50
Insulation	Equivalent insulation	1500	1000	0.2
Permanent magnets	NdFe35	7600	450	14
Air gap	Equivalent air	1.225	1006.43	0.0242
Housing	Aluminum	2700	900	200

ISSN: 2710-0588

For simplicity, the stator windings and insulation are represented by an equivalent thermal-conduction model. The laminated core is assigned anisotropic thermal-conductivity properties, with a lower axial thermal conductivity than radial thermal conductivity.

4. Results and Discussion

4.1. Design and Selection of Cooling Channels

For the interior-rotor permanent-magnet motor, two axial through-shaft cooling-channel designs are developed: a helical channel and a smooth channel. Their geometries are shown in Fig. 2.

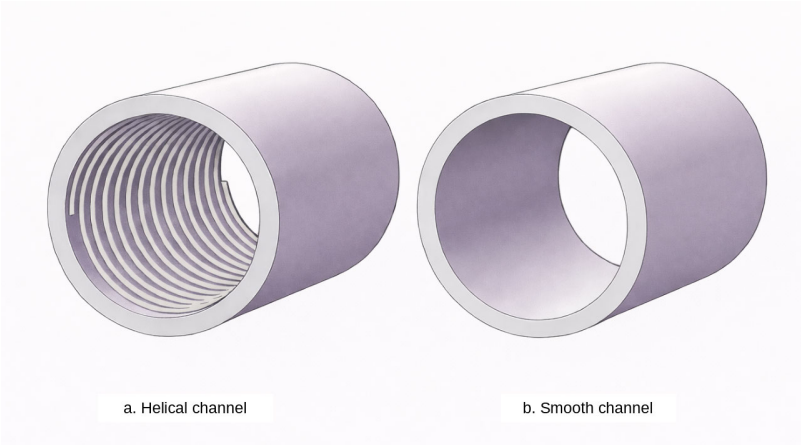


Figure 2. Geometries of the water-cooling channels

The two channel designs are compared using Ansys Fluent. For the flow boundary conditions, the channel inlet is defined as a velocity inlet at 25 °C and 1.3 m/s, while the outlet is defined as a pressure outlet at one standard atmosphere.

The static-pressure contours and velocity distributions for the helical and smooth channels are shown in Figs. 3 and 4. The two channel designs exhibit markedly different flow characteristics. In the smooth channel, static pressure decreases gradually along the axial direction, and the velocity vectors are largely aligned with the channel axis, indicating predominantly stable axial flow. Pressure loss is mainly due to wall friction, with relatively small local losses, resulting in favorable hydraulic performance. In contrast, the helical channel exhibits a steeper static-pressure gradient and noticeable periodic pressure fluctuations along the helical pitch. Its velocity streamlines show a pronounced swirling progression, indicating enhanced flow disturbance and secondary-flow formation. However, the helical geometry also increases local and frictional losses, leading to a larger overall pressure drop.

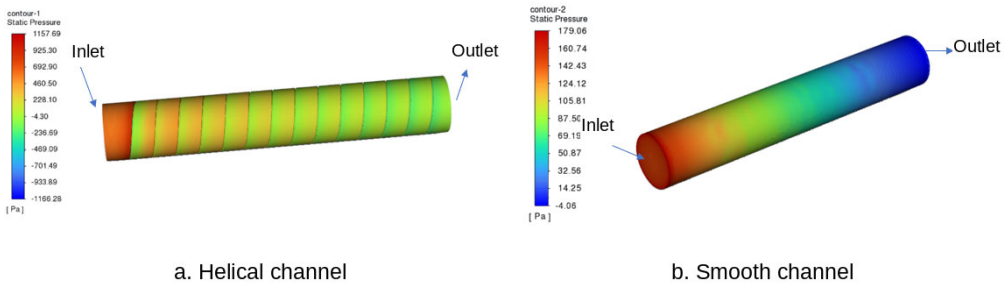


Figure 3. Static-pressure contours for the two channel designs

ISSN: 2710-0588

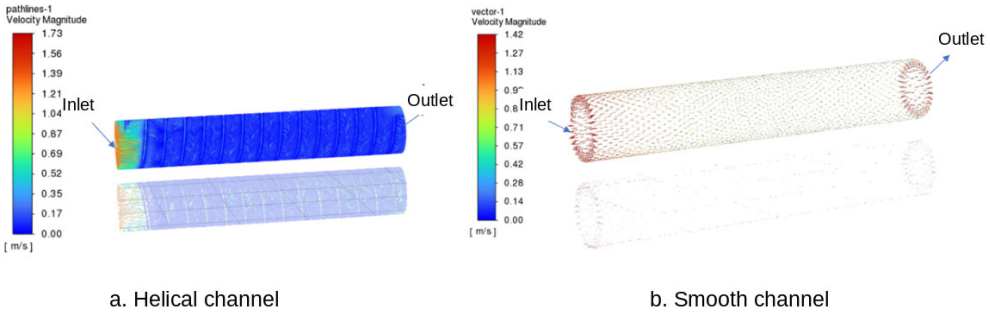


Figure 4. Velocity streamlines for the two channel designs

The smooth channel therefore offers the advantages of lower pressure drop, more stable flow, and higher axial transport efficiency. Although the helical channel can enhance fluid mixing, this enhancement comes at the cost of greater hydraulic losses.

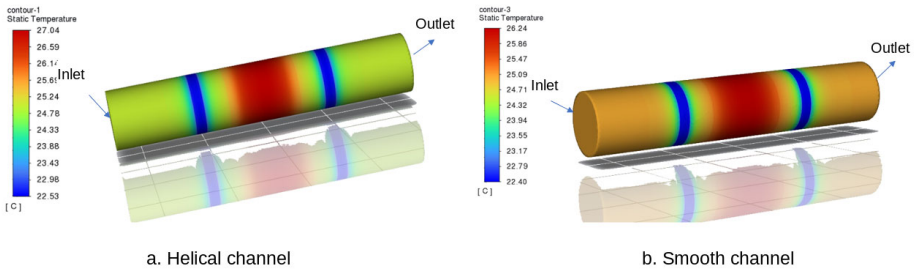


Figure 5. Temperature contours for the two channel designs

Figure 5 shows the temperature distributions of the two channel designs. Both structures develop a clear high-temperature region near the middle of the channel, but their temperature fields differ. The maximum temperature of the helical channel in Fig. 5(a) is 27.04 °C, higher than the 26.24 °C obtained for the smooth channel in Fig. 5(b), indicating weaker hotspot suppression. The high-temperature region in the middle of the helical channel is more concentrated and has a steeper temperature gradient, whereas the smooth channel exhibits a more gradual temperature distribution and a smaller overall temperature variation. This indicates better temperature-field uniformity. Under the conditions investigated, the smooth channel removes heat more effectively through more stable flow and therefore provides better overall cooling performance than the helical channel.

Table 4. Comparison of simulation results for the two water-cooling structures

Cooling-system parameter	Helical channel	Smooth channel
Inlet velocity ($m \cdot s^{-1}$)	1.3	1.3
Maximum velocity ($m \cdot s^{-1}$)	1.73	1.42
Velocity distribution	Nonuniform	Uniform
Maximum inlet–outlet pressure difference (Pa)	1058	163
Maximum temperature (°C)	27.04	26.24

ISSN: 2710-0588

As shown in Table 4, at the same inlet velocity, the smooth channel has a more uniform velocity distribution, a smaller inlet–outlet pressure difference, and a lower maximum temperature, indicating better overall hydraulic and cooling performance than the helical channel. Although the helical channel can intensify flow disturbances and increase local velocity, it introduces a substantially larger pressure drop and does not effectively reduce the maximum temperature. Therefore, the smooth channel has superior overall performance under the conditions studied.

4.2. Temperature-Field Analysis of the Hollow-Shaft Permanent-Magnet Motor

For comparison with the proposed hollow-shaft motor, the steady-state temperature field of a 60-mm-diameter solid-shaft permanent-magnet motor under constant-temperature seawater convective cooling is analyzed using Fluent. The temperature contours are shown in Fig. 6, and the maximum temperatures of key components are listed in Table 5. Without the hollow-shaft water-cooling structure, the maximum temperatures of the stator core, stator windings, permanent magnets, and shaft all exceed 247 °C, far above the allowable temperature limits of Class B insulation and the permanent magnets.

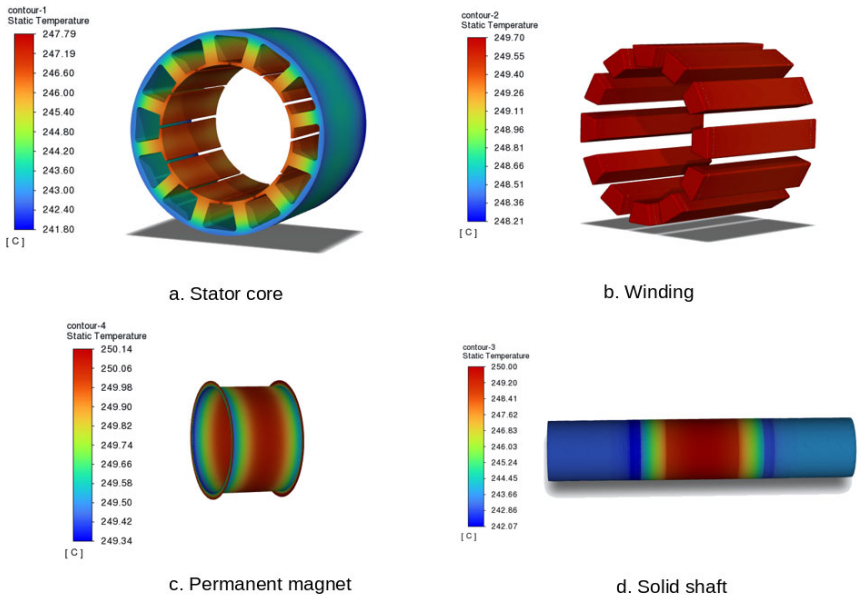


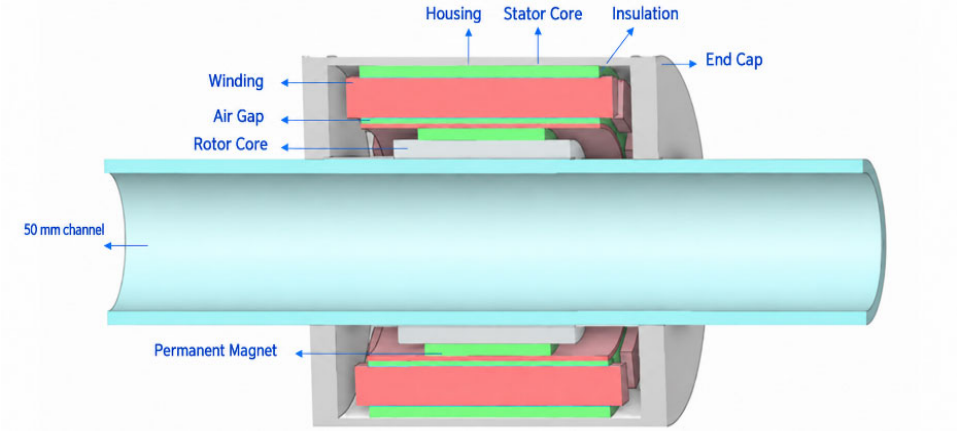
Figure 6. Temperature contours of key components in the 60-mm solid-shaft permanent-magnet motor

Table 5. Maximum temperatures of key components in the 60-mm solid-shaft permanent-magnet motor

Component	Stator core	Winding	Permanent magnet	Solid shaft
Maximum temperature (°C)	247.7	249.7	250.1	249.9

Using the previously selected smooth hollow-shaft design and maintaining the contact area between the coolant and the hollow-shaft wall, a motor with a 60-mm shaft diameter and a 50-mm cooling-channel diameter is constructed by changing the volume available for coolant inside the shaft, as shown in Fig. 7. Natural convection is applied to the housing and end covers, with the boundary temperature set to 20 °C. The coolant temperature is set to 25 °C and the inlet velocity to 1.3 m/s. The temperature field is calculated using Fluent, and the steady-state temperatures with the 50-mm cooling channel are listed in Table 6.

ISSN: 2710-0588



Figutr 7. Model of the permanent-magnet motor with a 50-mm smooth hollow-shaft cooling channel

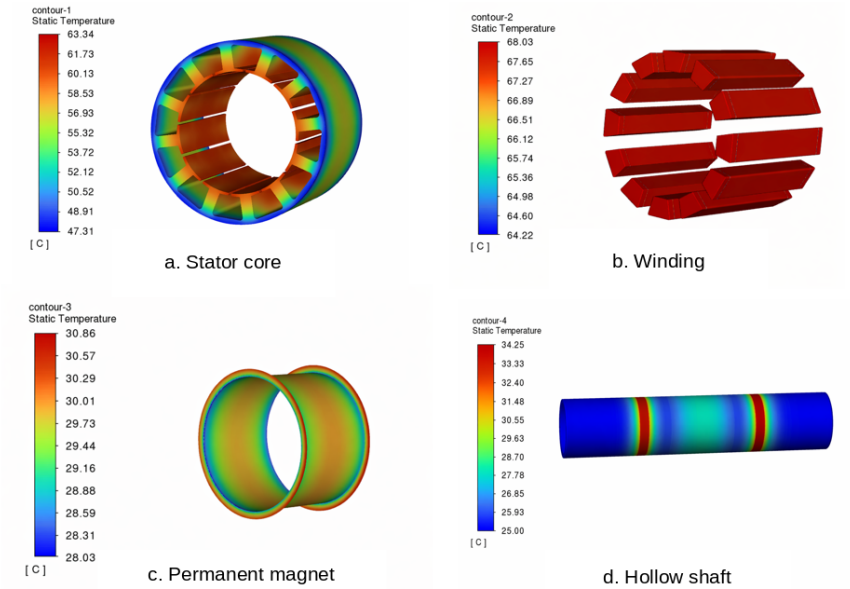


Figure 8. Temperature contours of the permanent-magnet motor with a 50-mm hollow-shaft cooling channel

Table 6. Maximum temperatures of key components in the permanent-magnet motor with a 50-mm cooling channel

Component	Stator core	Winding	Permanent magnet	Hollow shaft
Maximum temperature (°C)	63.34	68.03	30.86	34.25

As shown in Fig. 8 and Table 6, the hollow-shaft structure provides better heat dissipation than the solid-shaft structure. With the hollow shaft, the maximum temperatures of the stator core, windings, permanent magnets, and hollow shaft are 63.34 °C, 68.03 °C, 30.86 °C, and 34.25 °C, respectively. The rotor-side hot region is markedly reduced, and the axial temperature distribution becomes more uniform. Relative to the solid-shaft case, the maximum temperatures of the stator core, windings, permanent magnets, and shaft decrease by approximately 74.4%, 72.8%, 87.7%, and 86.3%, respectively. These results indicate that the hollow-shaft structure shortens the internal rotor heat-transfer path and reduces heat

ISSN: 2710-0588

accumulation near the rotor center, thereby mitigating local magnet overheating and the risk of demagnetization and supporting safe motor operation.

4.3. Effect of Cooling-Channel Diameter on Motor Temperature Rise

Using the smooth hollow-shaft water-cooling structure, the housing and end covers are assigned natural-convection boundaries at 20 °C, the coolant temperature is set to 25 °C, and the inlet velocity is fixed at 1.3 m/s. While keeping the motor's electromagnetic performance and coolant inlet velocity unchanged, the radial channel diameter is varied to investigate its effect on motor temperature rise. Figure 9 shows the relationships between channel diameter, maximum temperature, and maximum inlet–outlet pressure difference. As shown in Fig. 9(a), as the hollow-shaft channel diameter increases from 20 mm to 50 mm, the maximum temperatures of the permanent magnets, stator core, and windings decrease. This indicates that increasing the internal channel diameter enhances heat transfer on the rotor side, improves heat transport from the rotor region, and affects the overall temperature distribution. The winding temperature remains the highest and is therefore still a key target for temperature-rise control. Figure 9(b) shows that the maximum inlet–outlet pressure difference decreases from 441.91 Pa to 183.11 Pa, indicating that a larger channel diameter reduces flow resistance and pressure loss. Overall, the 50-mm channel performs best in reducing key-component temperatures and flow resistance among the diameters investigated.

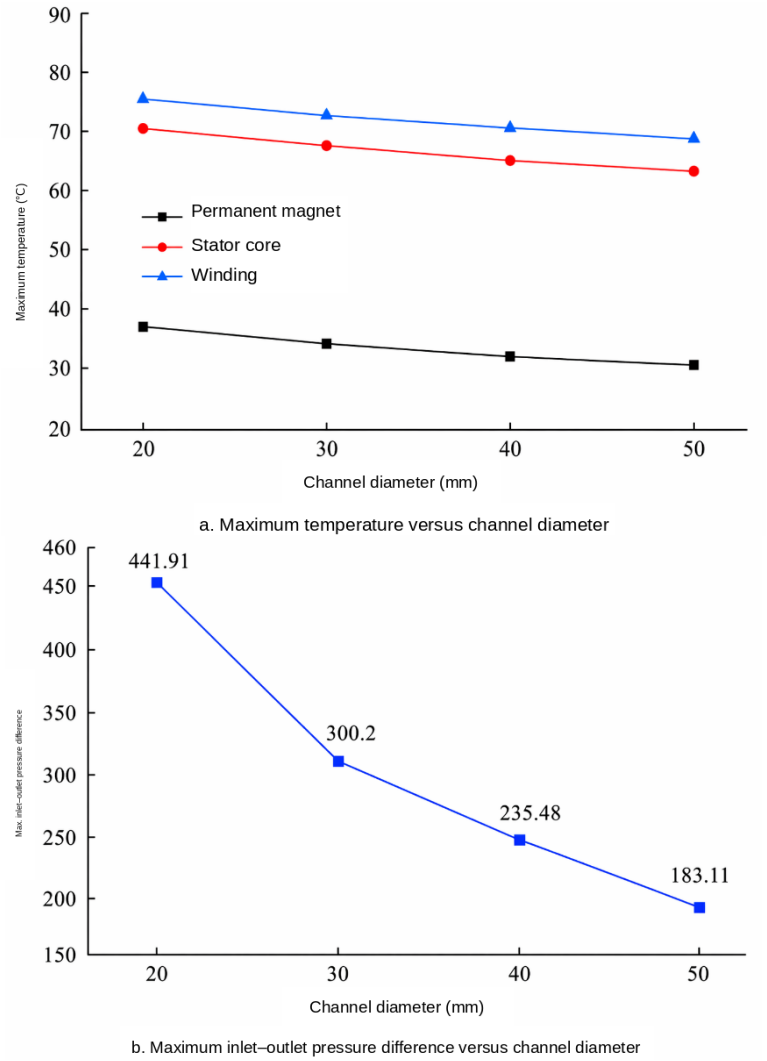


Figure 9. Effects of Channel Diameter on the Maximum Temperatures of Key Motor Components and the Maximum Inlet–Outlet Pressure Difference

ISSN: 2710-0588

4.4. Effect of Coolant Inlet Velocity on Motor Temperature Rise

With the channel diameter fixed at 50 mm and the coolant temperature at 25 °C, the inlet velocity is varied to investigate its effect on motor temperature rise. The corresponding results were intended to be shown in Fig. 10, which was not included in the supplied draft.

The maximum permanent-magnet temperature is fitted as a function of coolant inlet velocity; the coefficient of determination (R^2) is [value to be added].

5. Conclusions

A coupled electromagnetic-loss and temperature-field analysis is performed for an interior-rotor permanent-magnet motor to address insufficient heat dissipation on the rotor side. Two through-shaft cooling-channel designs—a helical channel and a smooth axial channel—are developed and compared in terms of flow and heat-transfer performance. The smooth-channel design is selected, and a three-dimensional water-cooled motor model is used to investigate the factors affecting the temperature field. The main conclusions are as follows:

1) At the same inlet velocity of 1.3 m/s, the smooth channel achieves a maximum temperature of 26.24 °C and a maximum inlet–outlet pressure difference of 163 Pa, compared with 27.04 °C and 1058 Pa, respectively, for the helical channel. The smooth channel therefore provides superior overall thermal–hydraulic performance under the investigated conditions.

2) Compared with the 60-mm solid-shaft motor, the 60-mm hollow-shaft motor with a 50-mm cooling channel reduces the maximum temperatures of the stator core, windings, permanent magnets, and shaft to 63.34 °C, 68.03 °C, 30.86 °C, and 34.25 °C, respectively. All values remain below the allowable temperatures of Class B insulation and the NdFe35 permanent magnets.

3) Increasing the cooling-channel diameter from 20 mm to 50 mm lowers the maximum temperatures of the permanent magnets, stator core, and windings and reduces the maximum inlet–outlet pressure difference from 441.91 Pa to 183.11 Pa. Thus, the 50-mm channel provides the best overall performance among the diameters investigated.

References

[1] Gundabattini, E., Mystkowski, A., Singh, R. R., & Gnanaraj, S. D. (2021). Water cooling, PSG, PCM, cryogenic cooling strategies and thermal analysis (experimental and analytical) of a permanent magnet synchronous motor: A review. Sādhanā, 46, Article 124. https://doi.org/10.1007/s12046-021-01650-z.

[2] Gai, Y., Kimiabeigi, M., Chong, Y. C., et al. (2019). Cooling of automotive traction motors: Schemes, examples, and computation methods—A review. IEEE Transactions on Industrial Electronics, 66(3), 1681–1692. https://doi.org/10.1109/TIE.2018.2835397

[3] Zhu, Z. Q., & Liang, D. (2022). Perspective of thermal analysis and management for permanent magnet machines, with particular reference to hotspot temperatures. Energies, 15(21), Article 8189. https://doi.org/10.3390/en15218189

[4] Usca-Gomez, H. G., Puma-Benavides, D. S., Zambrano-Leon, V. D., et al. (2025). A review and case study of cooling methods: Integrating modeling, simulation, and thermal analysis for a model based on a commercial electric permanent magnet synchronous motor. World Electric Vehicle Journal, 16(8), Article 437. https://doi.org/10.3390/wevj16080437

[5] Tang, Y., Sun, S., Yu, W., & Hua, W. (2023). Thermal analysis of water-cooling permanent magnet synchronous machine for port traction electric vehicle. Electronics, 12(3), Article 734. https://doi.org/10.3390/electronics12030734

[6] Jeon, K., Park, M., Park, J., et al. (2023). Analysis of cooling characteristics of permanent magnet synchronous motor with different water jacket design using electromagnetic–thermal fluid coupled analysis and design of experiment. Machines, 11(9), Article 903. https://doi.org/10.3390/machines11090903

ISSN: 2710-0588

[7] Zhao, H., Zuo, W., Li, Q., et al. (2023). Thermal–hydraulic performance optimization of the spiral cooling channel in surface type permanent magnet synchronous motor. Journal of Thermal Analysis and Calorimetry, 148(19), 10345–10355. https://doi.org/10.1007/s10973-023-12390-z

[8] Chen, W., Mao, Z., & Tian, W. (2024). Water cooling structure design and temperature field analysis of permanent magnet synchronous motor for underwater unmanned vehicle. Applied Thermal Engineering, 240, Article 122243. https://doi.org/10.1016/j.applthermaleng.2023.122243

[9] Wang, D. X., Wen, K., & Chen, G. (2025). Design and analysis of a water-cooling structure for a low-speed outer-rotor permanent magnet motor. Journal of Shenyang University of Technology, 47(4), 509–516. (In Chinese).

[10] Lee, K. H., Cha, H. R., & Kim, Y. B. (2016). Development of an interior permanent magnet motor through rotor cooling for electric vehicles. Applied Thermal Engineering, 95, 348–356. https://doi.org/10.1016/j.applthermaleng.2015.11.022

[11] Yang, Y., Bilgin, B., Kasprzak, M., et al. (2017). Thermal management of electric machines. IET Electrical Systems in Transportation, 7(2), 104–116. https://doi.org/10.1049/iet-est.2015.0050

[12] Lindh, P. M., Petrov, I., Semken, R., et al. (2016). Direct liquid cooling in low-power electrical machines: Proof-of-concept. IEEE Transactions on Energy Conversion, 31(4), 1257–1266. https://doi.org/10.1109/TEC.2016.2597059

[13] Khalesidoost, S., Faiz, J., & Mazaheri-Tehrani, E. (2022). An overview of thermal modelling techniques for permanent magnet machines. IET Science, Measurement & Technology, 16(4), 219–241. https://doi.org/10.1049/smt2.12099

[14] Nonneman, J., T'Jollyn, I., Vanhee, S., & De Paepe, M. (2023). Thermal modelling and validation of a direct rotor cooled permanent magnet electric machine. In Proceedings of the 2023 IEEE International Electric Machines & Drives Conference (IEMDC). San Francisco, USA. https://doi.org/10.1109/IEMDC55163.2023.10238978

[15] Petrov, I., Credo, A., Canseven, H. T., et al. (2025). Direct liquid cooling in compact machines: Advantages and limitations. Applied Thermal Engineering, 273, Article 126461. https://doi.org/10.1016/j.applthermaleng.2025.126461